Rare Metal Materials and Engineering
Volume 51, Issue 12, December 2022
Available online at www.rmme.ac.cn

Science Press

Cite this article as: Shao Yingkai, Li Xiaoyan, Chen Li, et al. Investigation on Microstructure and Microtexture of Laser-Welded 2A97-T3 Al-Li Alloys by EBSD[J]. Rare Metal Materials and Engineering, 2022, 51(12): 4464-4474.

ARTICLE

Investigation on Microstructure and Microtexture of Laser-Welded 2A97-T3 Al-Li Alloys by EBSD

Shao Yingkai[1], Li Xiaoyan[1], Chen Li[2], Ji Gang[3]

[1] Faculty of Materials and Manufacturing, Beijing University of Technology, Beijing 100124, China; [2] China Aeronautical Manufacturing Technology Research Institute, Beijing 100124, China; [3] University Lille, CNRS, INRAE, Centrale Lille, Lille F-59000, France

Abstract: The laser-welded 2A97-T3 aluminum-lithium (Al-Li) alloy joints were sampled from upper horizontal surface, transverse section, longitudinal section, and lower horizontal surface to develop the comprehensive and spatial understandings for microstructure and microtexture evolution. Various characterization methods in terms of electron backscattered diffraction such as orientation imaging microscopy, pole figure, inverse pole figure, misorientation angles distribution, orientation distribution function, and numerical simulation were used. The results show obvious differences in the grain morphology, orientation, and microtexture in different areas of the joint, due to the nonequilibrium characteristic of cold rolling and laser beam welding. The laser beam can induce the formation and growth of dynamic recrystallization and sub-structure grains in the heat affected zone. Moreover, the original microtexture characteristics of the base metal is weakened and thus eliminated in both the heat affected zone and the weld zone.

Key words: laser beam welding; Al-Li alloy; electron backscattered diffraction; microstructure; microtexture

Due to outstanding properties such as excellent specific strength, stiffness and good corrosion resistance, aluminum-lithium (Al-Li) alloys are highly attractive for their lightweight structure in aircraft as well as for low- and medium-temperature performance improvement of materials in aerospace, military, and civil engineering industries[1,2]. For example, 2A97 Al-Li alloy, as one of the most representative third-generation Al-Li alloys developed by China, has demonstrated appreciable weldability, fracture toughness, and ductility compared to conventional commercial Al-Li alloys[3].

The principle driving force for further development of Al-Li alloys stems from the continuous industrial requirements for mass reduction and elastic modulus improvement by adding Li element to the Al-based alloy[4,5]. Moreover, the mass reduction of airframes made of Al-Li alloy can also be achieved by replacing riveting with welding, which can minimize mass gain due to the abundant overlapping joints[6]. Compared with traditional arc welding process, laser beam welding (LBW) has become increasingly attractive for welding Al-Li alloy due to its advantages including tight focus ability, high power density, flexible manufacturing, and outstanding automation[7-10]. LBW is featured with a sharp focus, a low heat input, and a rapid cooling rate so that the laser beam can easily penetrate relatively thick joints, forming a fine-grained weld with limited deformation and a narrow heat affected zone (HAZ). The latter leads to the negligible influence of HAZ softening on tensile strength of the joints[11]. Thus, the overall mechanical properties of LBW joints are more pronounced compared with those of the joints formed using arc welding processes with a lower power density, showing a good application potential[11-13].

During LBW, microstructure evolution from base metals (BM) to joint is significant mainly due to rapid heating/cooling, which has a direct impact on mechanical properties to determine quality of the welded joint. Regard to this, electron backscatter diffraction (EBSD) provides a useful tool since texture measurement[14], microstructure quantification[15], phase partitioning[16], grain and phase boundary characterization[17], and strain analysis[18] of a polycrystalline material can be statistically carried out by this technique. Till date, the studies of 2A97 Al-Li alloys are mainly focused on friction stir welding[3,19] and corrosion behavior[20,21]. In these studies,

Received date: January 24, 2022
Foundation item: Supported by Project (614290801051809)
Corresponding author: Li Xiaoyan, Ph. D., Professor, Faculty of Materials and Manufacturing, Beijing University of Technology, Beijing 100124, P. R. China, Tel: 0086-10-67391856, E-mail: xyli@bjut.edu.cn

EBSD is mainly used to explore the microstructure evolution of solid-state phase transformation, determine the corrosion position of BM, and characterize the phase distribution of weld zone. However, few data on the crystallographic texture of LBW joints of 2A97 Al-Li alloy are available[22]. It is noteworthy that microtexture often causes anisotropic mechanical properties. Although significant research efforts[23-26] have been devoted to study the considerable deformation textures in Al-Li based alloys, these researches are often restricted to the observation only in a single section. Considering the directionality of microtexture, the investigations on orientations and volume fractions of different textures along different directions and in three dimensions are necessary.

In this study, by sampling the upper horizontal surface, transverse section, longitudinal section, and lower horizontal surface of the joint (Fig. 1a), EBSD was performed to study microstructures and microtextures in different regions of the 2A97-T3 LBW joints in order to clarify the relationship between microstructure evolution and thermal cycle. The underlying mechanism related to microstructure and microtexture evolutions of the joint was discussed by optical microscopy (OM), EBSD, and numerical simulation.

1 Experiment

2A97-T3 Al-Li alloy sheets with 1.2 mm in thickness and ER2319 wire with 1.2 mm in diameter were used as the BM and filler wire, respectively. Their chemical compositions are listed in Table 1.

The schematic illustration of LBW device is presented in Fig. 1a. LBW system (IPG YLS-5000) equipped with an industrial robot (ABB IRB2400 M2000) was utilized parallel to the rolling direction. The experiment was conducted with the laser power of 1.4 kW, the travel speed of 2.1 m·min^{-1}, and the filler wire feeding speed of 2.0 m·min^{-1}. Root shielding was carried out by purging 99.9% argon before welding and then supplying the gas at a flow rate of 10 L·min^{-1} through equidistant holes to ensure the stable and uniform gas flow. The face shielding gas was fed through a trailing torch and a gas nozzle coaxial to filler wire, with the flow rate of 15 and 10 L·min^{-1}, respectively.

In order to perform EBSD analysis along the three orthogonal directions including rolling direction (RD), transverse direction (TD), and normal direction (ND), samples were taken from upper horizontal surface, transverse section, longitudinal section, and lower horizontal surface of the selected joint according to the principle shown in Fig. 1b, which are marked by red solid line frame and red dotted line frame in Fig. 1a. These samples contain regions of BM, HAZ, and weld zone, which are convenient to observe the microstructures and microtextures of the laser welded 2A97-T3 joint. EBSD was carried out using a Tescan MAIA3 scanning electron microscope operated at 20 kV. The step size of EBSD analysis was set to 1.5 μm. Sequential preparation steps of EBSD specimens include mechanical polishing with 2.0, 1.0, and 0.5 mm diamond suspension, followed by vibration polishing with 0.02 mm colloidal silica for 15 min by a VibroMet 2 polisher. Moreover, in order to acquire reliable data, the measurement of as many grains as possible was required and some special data-hindering parameters (such as noise, incomplete grains at the edge of the image) were removed. EBSD data were post-treated by the HKL Channel 5 software. The Vickers microhardness test was performed over the transverse section in the middle part using a 0.98 N load for 15 s to obtain the hardness profiles.

2 Numerical Simulation

2.1 Three-dimensional modeling and meshing

Fig. 2a illustrates that due to the adoption of the plate butt process, the two sheets along the weld centerline are symmetrical in welding direction. Therefore, a semi-model with only one experimental sheet was established for meshing and analysis. Considering the laser beam heating, the region closer to the keyhole is more sensitive to the welding thermal cycle. Consequently, in order to improve the accuracy and

Table 1 Chemical compositions of 2A97-T3 BM and ER2319 filler wire (wt%)

Material	Cu	Mg	Li	Zr	Ag	Fe	Mn	Zn	Si	Al
2A97-T3	3.9	0.42	1.4	0.15	0.24	0.12	0.3	0.44	-	Bal.
ER2319	5.6	0.02	-	0.18	-	0.3	0.3	0.10	0.20	Bal.

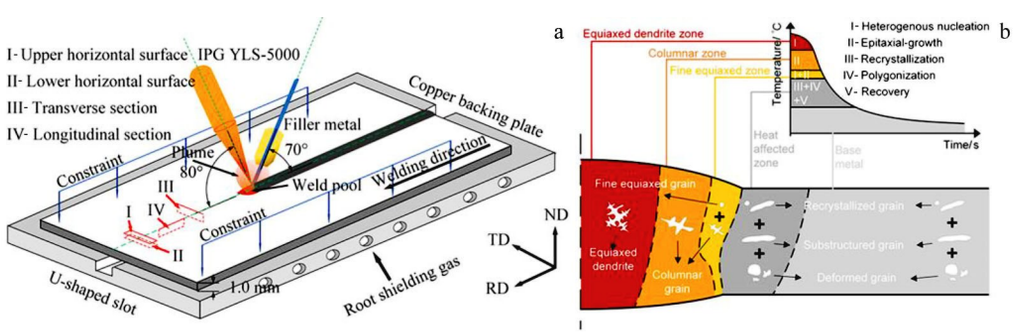

Fig.1 Schematic illustration of laser beam welding device (a) and sample selection (b)

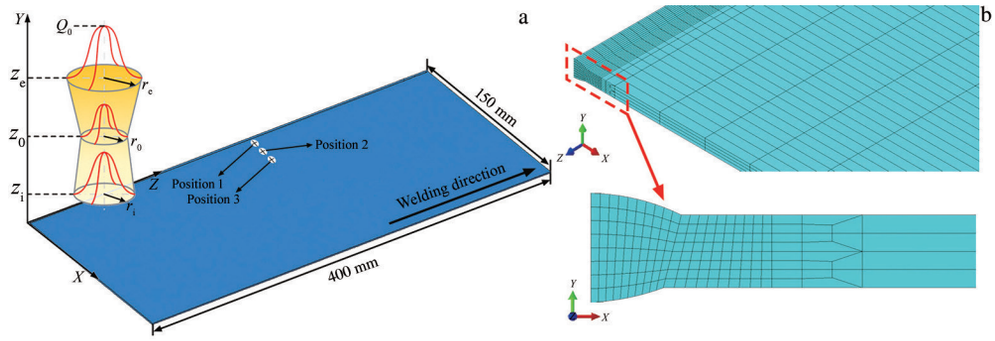

Fig.2 3D semi-model of the butt joint and hourglass-like heat source (a) and mesh of the model and high-magnification image of mesh in weld zone and HAZ (b)

efficiency of simulation, a fine mesh size was selected in the weld zone and the HAZ. On the other hand, a coarse mesh size is more suitable for BM which is far away from the keyhole[23]. The element type to mesh the three-dimensional (3D) model is an 8-noded hexahedron, i.e. DC3D8, and the smallest and the biggest element dimensions are 0.12 mm×1 mm×0.15 mm and 5 mm×1 mm×0.3 mm, respectively (Fig. 2b). The temperature-dependent thermal properties are obtained from the third-generation Al-Li 2198 alloy, which possesses the compositions similar to the 2A97 alloy[24].

$$Q_v = \begin{cases} \dfrac{9Q_0 e^3}{\pi(e^3-1)} \times \dfrac{1}{(z_e - z_0)\left(r_e^2 + r_e r_0 + r_0^2\right)} \exp\left(-\dfrac{3r^2}{r_{c1}^2}\right) & z \geqslant z_0 \\ \dfrac{9Q_0 e^3}{\pi(e^3-1)} \times \dfrac{1}{(z_0 - z_i)\left(r_0^2 + r_0 r_i + r_i^2\right)} \exp\left(-\dfrac{3r^2}{r_{c2}^2}\right) & z < z_0 \end{cases} \quad (1)$$

where $Q_0 = \eta P$ is the laser welding input power; η is the utilization ratio of laser energy; P is the laser welding power; the subscripts of e, 0, and i represent the top, middle, and bottom surfaces of the heat source, respectively; r and z are the radius and height of the heat source surface; respectively, and $r_{c1} = r_0 + (r_e - r_0)\dfrac{z - z_0}{z_e - z_0}$, $r_{c2} = r_i + (r_0 - r_i)\dfrac{z - z_i}{z_0 - z_i}$.

2.3 Boundary conditions

The symmetric plane of the 3D semi-model and the root of the joint were set to be adiabatic. The bottom surface of the sheet was considered to be in contact with the steel due to the existence of the backing plate. Moreover, the remaining surfaces are assumed to be heat radiating surfaces with stagnant ambient air directly. The heat flux from the inner side of the object to its boundary surface is equal to the heat flux from the boundary surface to the steel plate and ambient air. Therefore, only the heat loss of surface-to-surface contact and surface radiation are considered, and their equivalence coefficients are set to be 3.0 and 0.8, respectively. From the thermodynamic perspective, the variation of specific heat capacity from top to bottom of the keyhole leads to different utilization rate of laser energy. Therefore, the average value is adopted to simplify the calculation. Moreover, from the perspective of heat source model, the use of combined heat source model also needs to adjust the utilization ratio of laser energy. For example, when the filler wires are incorporated on the upper surface of the molten pool, the heating radius of the laser beam (0.5 mm in this study), the insulation effect of argon shielding gas at the joint root, and boundary effect of the keyhole must be considered when selecting size parameters of the heat source model. In this study, the optimized size parameters of the hourglass-like heat source are obtained and listed in Table 2 based on the above-mentioned analysis.

Moreover, the same parameters as those of the BM are applied to the weld zone as well.

2.2 Heat source model

The deep penetration mode of LBW was used in this study, and the hourglass-like hybrid heat source (Fig. 2a) was selected based on the actual morphology of the weld zone. The hourglass-like heat source can be regarded as a combination heat source of two conical heat sources, and the power function of the hourglass-like heat source can be represented as follows [25]:

2.4 Thermal cycle measured by thermocouple

In order to verify the accuracy of temperature field results of numerical simulation, thermocouples were used to measure thermal cycles at different positions in heat affected zone and base metal during laser welding process. The measuring positions 1~3 are shown in Fig. 2a, which are 2, 3.5, and 7.5 mm away from the weld center, respectively.

3 Results and Discussion

3.1 Temperature field of heat affected zone and base metal

The main objective of simulating the temperature field of LBW is to obtain thermal outputs in order to further analyze the evolution mechanism of microstructure during this thermal

Table 2 Optimized parameters of the hourglass-like heat source in the simulation

Parameter	η	z_e	z_0	z_i	r_e	r_0	r_i
Value	0.21	1.2	0.8	0.0	1.5	0.5	0.4

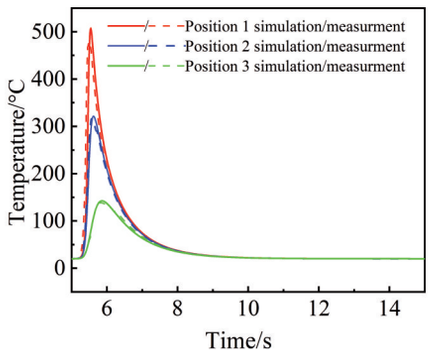

Fig.3 Comparison between simulated and measured thermal cycles

processing. Thus, verification of the accuracy of temperature gradient is very important. First, the comparison between simulated and measured thermal cycles is shown in Fig.3, and it can be seen that the simulated values agree with the measured ones. Second, the liquid temperature of 2A97 alloy is set to 630 ° C, and Fig. 4a compares the numerically predicted temperature contours with the geometrical features of frozen molten pool by transverse section of the joint. Clearly, variation tendency of the temperature contours exhibits a good match with the transverse section of the joint. Furthermore, to verify the width of HAZ of thermal simulation, the corresponding microhardness distribution of joint was investigated. For heat-treated Al alloys, a decrease in hardness occurs in the area of the BM near the weld zone, which is considered to approximate the HAZ. The width of HAZ measured from the microhardness profile is in good agreement with the simulated size. It is noted that the width of the numerically predicted HAZ is determined based on the temperature range of 400~630 ° C for Al-Cu alloys[26, 27]. In summary, the simulation results are verified from multiple aspects, which are in good agreement with the experimental results, indicating that the simulation temperature field is accurate. The simulation temperature histories of nodes 1~9 are presented in Fig.4b and 4c. The thermal history curves of these nodes along the longitudinal distribution near the fusion line are similar, with high peak temperature and long high-temperature residence time. In contrast, with the increase in the distance from the weld zone, the peak temperature of thermal history curves of nodes decreases rapidly, and the high temperature residence time is also very limited.

3.2 Laser beam welding-induced microstructural evolution

EBSD measurements were conducted at different regions including upper horizontal surface, transverse section, longitudinal section, and lower horizontal surface of the laser welded 2A97-T3 Al-Li alloy joint, whose macroscopic morphology is shown in Fig.5. The detailed information about the macro- and micro-structure formation mechanism of the weld zone is presented in our previous studies[1,28]. Furthermore, the EBSD results including OIM, PF, IPF, misorientation angles distribution, ODF, and grain morphology map are obtained as shown in Fig.6~12.

Fig. 6a shows the OIM of upper horizontal surface orderly consisting of BM, HAZ, fine equiaxed zone, columnar zone, and equiaxed dendrite zone from right to left. In BM, the grains present a pancake-like shape and are elongated along the rolling direction. The OIM is predominately blue corresponding to the associate <111> oriented grains, and a slight color difference between these grains indicates the

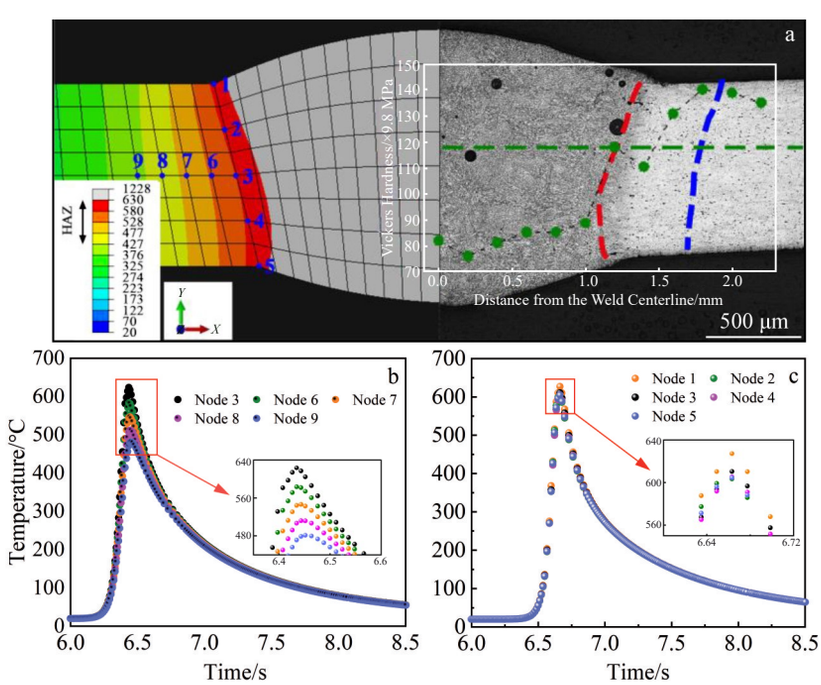

Fig.4 Results of numerical simulation: (a) comparison of the numerically predicted and experimentally measured weld zone and HAZ of the joint from transverse section and microhardness profile; (b, c) simulation thermal history curves at nodes 1~9

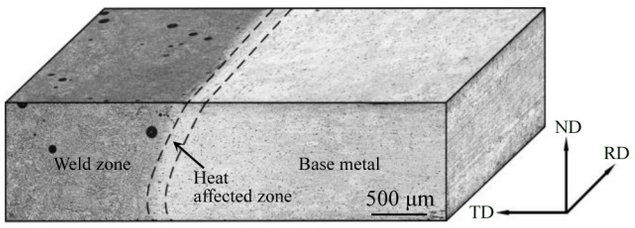

Fig.5 Triplanar macroscopic morphology illustrating the structure of laser welded 2A97-T3 Al-Li alloy joint

existence of numerous substructures in their interiors. Furthermore, a small fraction of grains in other colors are also observed corresponding to intermediate orientations. Therefore, the microstructure of BM is characterized by some preferred orientations. Compared with BM, HAZ presents similar colors and shapes of grains, demonstrating that HAZ also has the same preferred orientations and change in the microstructures is seldom observed. In weld zone, equiaxed dendrite zone and fine equiaxed zone are rich in different colors, indicating that their grain orientation is significantly random. The grains of columnar zone exhibit a flat shape and they are almost all red, which indicates that the grains in this region grow along <100> preferred orientation. This is consistent with the theory that columnar dendrites grow along the <100> heat dissipation direction. Consequently, under the action of LBW, the microstructures of weld zone change significantly compared with those of BM and HAZ.

Fig. 6b demonstrates that PF of BM exhibits a typical rolling texture for face-centered-cubic materials, and this rolling texture intensity of HAZ is reduced significantly[14]. Moreover, in columnar zone, PF of {100} exhibits a strong intensity of preferred orientation corresponding to its OIM. PFs in equiaxed dendrite zone and fine equiaxed zone exhibit low intensity and irregular distribution, indicating that no obvious texture is developed in both regions.

The corresponding IPFs of BM, HAZ, and columnar zone (CZ) are shown in Fig.6c to further analyze their microtexture characteristics. In the BM, <112>, <111>, <101> are parallel to *Y*0 (RD), *X*0 (TD), and *Z*0 (ND), respectively, and intensities of these orientation relationships also decrease gradually. Except <111>, orientation relationships of <112> and <101> change significantly in the HAZ. The existence of these orientation relationships verifies the viewpoint that there is preferred orientation in the BM and HAZ as shown in Fig. 4a. Moreover, for IPFs of columnar zone, the <100> orientation is obviously parallel to *X*0, which proves the fiber texture characteristic of columnar grains growing again along

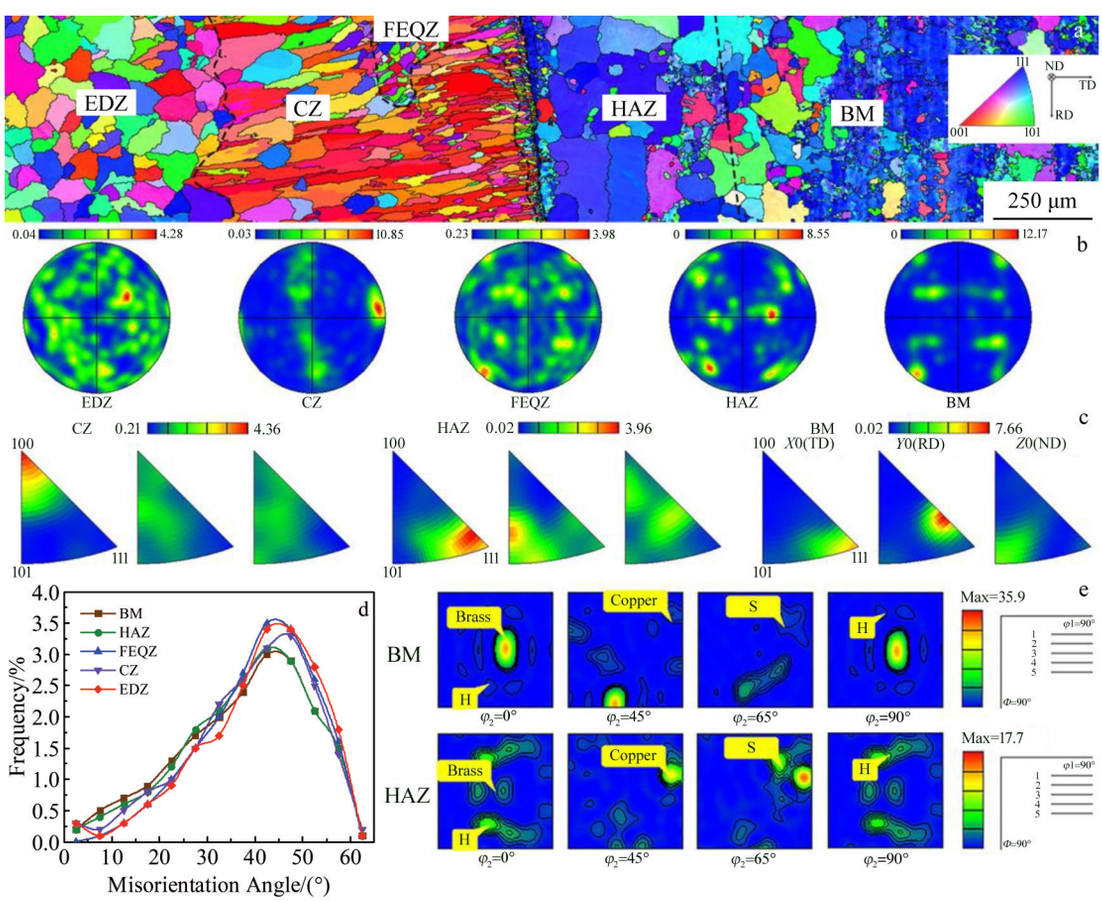

Fig.6 EBSD results of base metal (BM), heat affected zone (HAZ), fine equiaxed zone (FEQZ), columnar zone (CZ), and equiaxed dendrite zone (EDZ) from the upper horizontal surface of the joint: (a) OIM, (b) PFs of {100}, (c) IPFs, (d) misorientation angle distributions, and (e) ODFs

the solidification direction.

Fig. 6d shows that the misorientation angles of equiaxed dendrite zone and fine equiaxed zone are mainly concentrated in the range of 40°~50°, indicating that these regions possess randomly orientated grains and good isotropy. However, the misorientation angles of remaining regions exhibit obvious distribution at less than 15°, and their fraction order from the most to the least is BM, HAZ, and columnar zone. This phenomenon demonstrates the existence of anisotropic characteristic, i.e. microtexture, in these regions.

To sum up, the microtexture feature of upper horizontal surface is significantly distinct. Therefore, it is necessary to use ODFs to determine the specific microtexture, which are usually represented by sections with φ_2 of 0°, 45°, 65°, and 90° (Fig.6e). The ODFs of BM reveal an obvious cold rolling texture, so-called β-fiber composed of brass {110}<112>, copper {112}<111>, and S{123}<634>[14, 19]. Among these components, brass orientation exhibits the greatest intensity. Moreover, the presence of weak H-component {100}<011> is closely related to the cold rolling process of thin sheets[29, 30]. In this process of cold rolling, in particular, for thin sheets, the upper and lower horizontal surfaces in contact with the rolling cylinders are subjected to large shear stresses, leading to the formation of H-component with shear texture[15]. From BM to HAZ, the intensity of β-fiber decreases with the dominant orientation changing from brass to copper, which is in good agreement with the intensity variation trend of orientation relationship shown in Fig.4c. Finally, the H-component is also present in HAZ with little changes.

The grain morphology maps of BM and HAZ are shown in Fig. 7. The proportions of different grain types and average grain sizes in BM and HAZ from all experimental surfaces are listed in Table 3. BM is mostly composed of deformed grains with a large number of low-angle grain boundaries within their interiors, featured with sub-structure grains and a small fraction of recrystallized grains. In HAZ, the proportion of deformed grains and low-angle grain boundaries decreases significantly. However, the proportion variation trend of other grains and high-angle grain boundaries is opposite, and the sub-structure grains increase notably. Moreover, the average grain size in HAZ becomes slightly larger compared to that in BM.

Fig.8 exhibits that the microstructures of transverse section have many similarities to that of upper horizontal surface; however, some differences also exist. Next, each of the differences is highlighted and the similarities are not repeated. Fig.8a shows the results of OIM, revealing that the upper and lower parts of BM and HAZ are characterized by coarse-laminated grains with a predominantly green and a small amount of pink, indicating the formation of H-component on the upper and lower parts of thin sheet. In the middle part of BM and HAZ, fine-broken grains with remarkable rolling characteristics are predominantly <111> oriented blue grains. The distribution range of equiaxed dendrite zone and fine equiaxed zone of transverse section increase slightly; however, the morphology and orientation are similar to those of upper horizontal surface. Nonetheless, in the columnar zone, the distribution is significantly reduced, but the <100> preferred orientation exhibits little change. For BM and HAZ, the rolling texture feature not only appears in Fig.8b, but also becomes more prominent. The differences in intensity distributions of PFs between Fig.6b and Fig.8b are caused by the transformation of observed surface, and it is the existence of such a difference that deepens the understanding of the distribution of microtextures. Based on the above-mentioned perspective, it is easy to understand the phenomenon of orientation relationship retained; nonetheless, the difference of intensity distribution is observed in Fig. 8c. Fig. 8d illustrates that the distribution trend of misorientation angles in each zone of the transverse section microstructure is similar to that

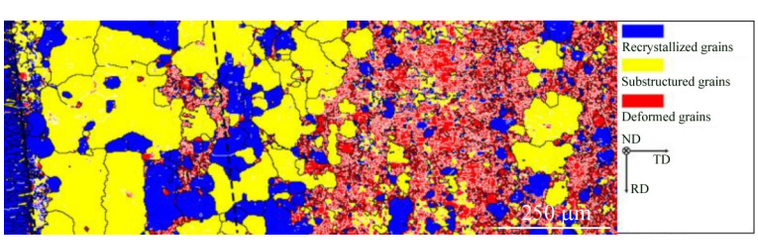

Fig.7 Grain morphologies map of BM and HAZ from the upper horizontal surface of the joint with high-angle grain boundaries (>15°) and low-angle grain boundaries (2°~15°) marked in black and white lines, respectively

Table 3 Proportions of different grain types and average grain sizes in BM and HAZ from upper horizontal surface (UHS), transverse surface (TS), and lower horizontal surface (LHS)

Proportion and grain size	UHS		TS		LHS	
	BM	HAZ	BM	HAZ	BM	HAZ
Recrystallized grain proportion/%	16.66	29.15	26.67	32.77	18.91	29.98
Sub-structure grain proportion/%	22.19	62.25	36.36	43.32	58.73	67.84
Deformed grain proportion/%	61.15	8.60	36.97	23.91	22.36	2.18
Average grain size/μm	11.76	17.08	12.45	14.62	14.62	17.24

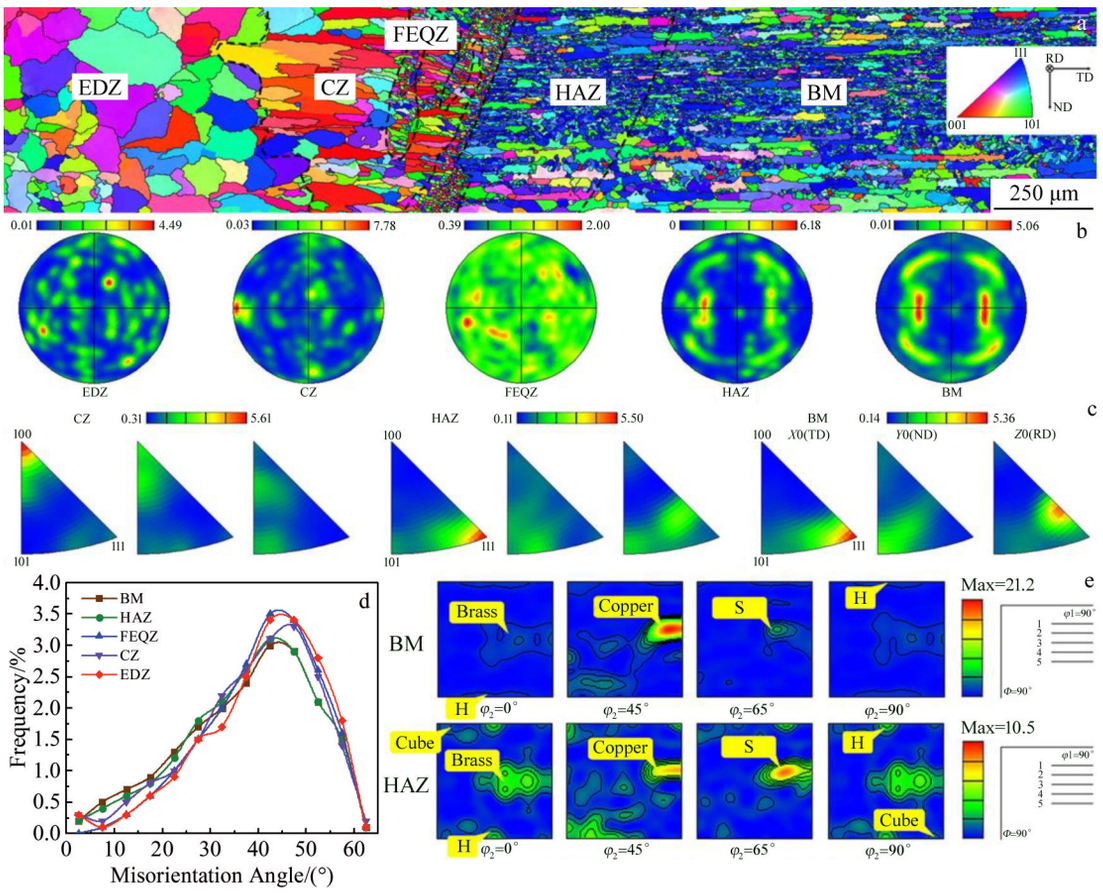

Fig.8 EBSD results of BM, HAZ, FEQZ, CZ, and EDZ from the transverse section of the joint: (a) OIM, (b) PFs of {100}, (c) IPFs, (d) misorientation angles distributions, and (e) ODFs

of the upper horizontal surface, which provides strong evidence to prove the existence of anisotropic or isotropic characteristic. ODFs of transverse surface are shown in Fig. 8e, and a new weak texture, cube-component {100}<001>, appears in the HAZ, except as described β-fiber and H-component[30-32]. The presence of cube-component may be related to the dynamic recrystallization under the welding thermal cycle. The dominant component of β-fiber in BM changes from brass to copper, which corresponds to the IPF of BM shown in Fig.7c.

Fig. 9 illustrates that the coarse grains mainly including recrystallized and sub-structure grains are concentrated in the upper and lower parts of the transverse section, and middle part is dominated by fine and broken deformed grains. This distribution phenomenon of grains is related to large plastic deformation, which is consistent with the above-stated cold rolling theory of thin sheets to form H-component[3]. Combined with the results presented in Table 3, the phenomenon is still observed in the HAZ that the number of deformed grains and low angle grain boundaries decreases while the number of sub-structure grains and recrystallized grains increases. Moreover, the closer to the weld, the more obvious this phenomenon is, and the average grain size of the HAZ is slightly reduced.

Fig. 10 demonstrates that OIM, PF, and misorientation angles of longitudinal section exhibit significant isotropic characteristics, such as a quantity of equiaxed dendrites, random crystal orientations, and large misorientation angles.

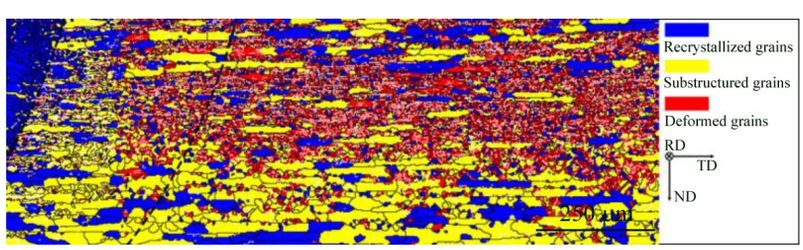

Fig.9 Grain morphologies maps of BM and HAZ from the transverse section of the joint with high-angle grain boundaries (>15°) and low-angle grain boundaries (2°~15°) marked in black and white lines, respectively

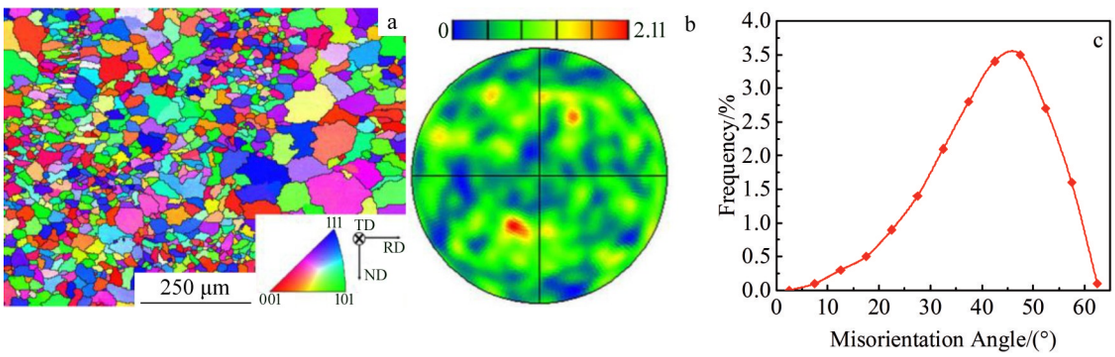

Fig.10 EBSD results of equiaxed dendrite zone from the longitudinal section of the joint: (a) OIM, (b) PF, and (c) misorientation angles distribution

The longitudinal surface is taken from the center line of the weld, which is the common end position of solidification from the edge to the center in the molten pool. It is the particularity of its position that creates the outstanding uniform microstructure.

Through the OIM of lower horizontal surface shown in Fig. 11a, the proportion of <110> oriented grains in the BM and HAZ increases, and the overall size of the weld zone decreases obviously. Moreover, the distributions of equiaxed dendrite zone and fine equiaxed zone increase significantly, while the characteristics of distribution and preferred orientation of columnar zone are weakened. The changes in orientation relationship can be more intuitively observed in the form of intensity distribution presented in Fig.11b and 11c, which is generally manifested in the weakening of the rolling texture characteristic of BM and HAZ and preferred orientation characteristic of columnar zone. The analysis methods of PFs and IPFs are the same as those of other surfaces, so they are not repeated herein. Fig.11d exhibits that the misorientation angle distribution of columnar zone is close to that of equiaxed zone and fine equiaxed zone, which also provides strong evidence for the weakening of orientation

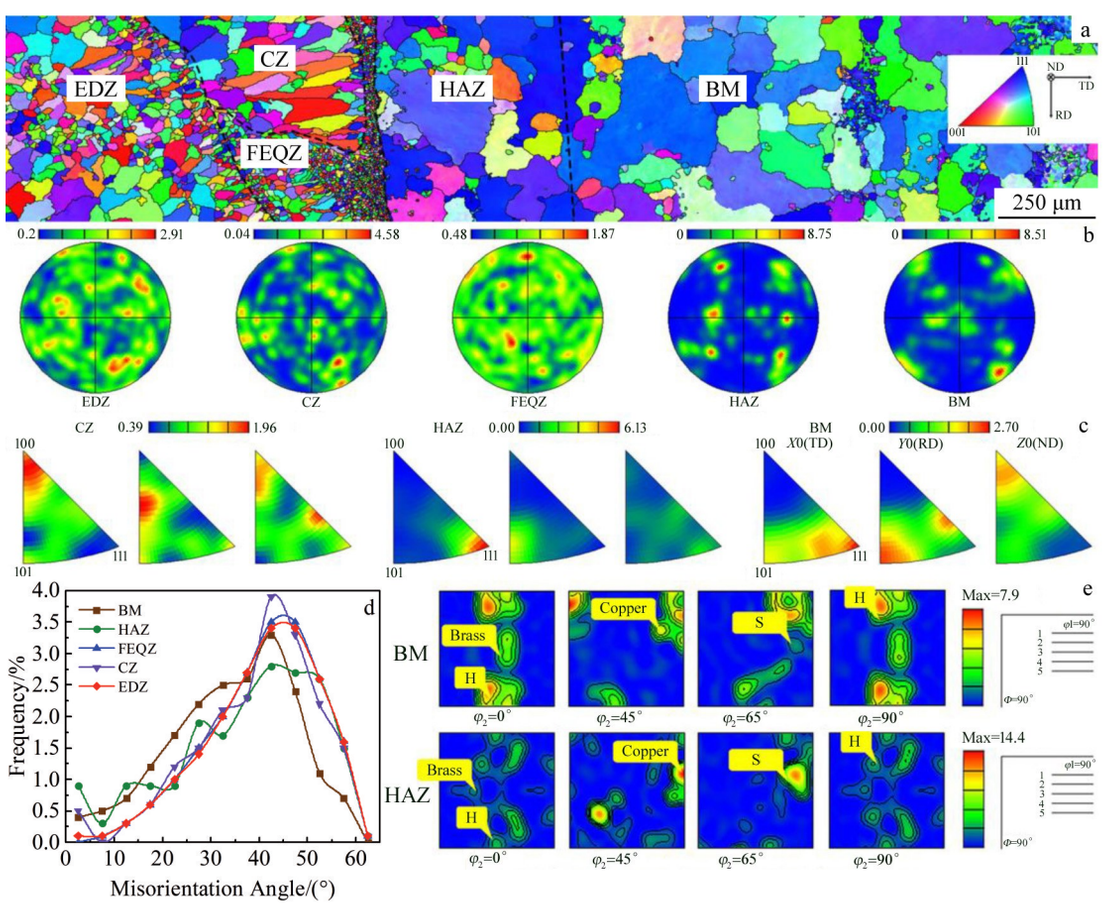

Fig.11 EBSD results of BM, HAZ, FEQZ, CZ, and EDZ from the lower horizontal surface of the joint: (a) OIM, (b) PFs of {100}, (c) IPFs, (d) misorientation angles distributions, and (e) ODFs

relationship. Furthermore, the BM and HAZ still exhibit obvious distribution within the misorientation angles less than 15° , which reveals that although the rolling texture is weakened, other textures still exist. The appearance of high-intensity H-component in ODFs (Fig. 11e) well explains the misorientation angle distributions of BM and HAZ.

The grain morphology map of lower horizontal surface is dominated by sub-structure grains, featured with recrystallized grains, and the number of deformed grains is very limited (Fig. 12). During the thin sheet cold rolling process, the strain is released periodically due to the formation of sub-structure grains and recrystallized grains, and this grain distribution is consistent with the high intensity of H-component[15, 30].

The microstructures of different surfaces of the joint exhibit corresponding characteristics, and the reasons can be attributed to the following two aspects: different observation views and cold/hot working process. Next, the microstructures and evolution mechanism of BM, HAZ, and weld zone were investigated from these two aspects.

First, the BM has obvious microtexture characteristics including β-fiber components and H-component, which exhibit some specific orientation relationships with the rolling direction and rolling surface. Further, these specific orientation relationships lead to corresponding changes in EBSD results when observed from different surfaces of the joint. Specifically, the H-component is generated in the contact surfaces between the sheet and the rolling cylinders during the cold rolling process[29]. Consequently, the H-component characteristics are obvious when testing the upper and lower horizontal surfaces, which highlights the characteristics of sheet thickness in cold rolling process. However, the transverse section contains whole areas from the upper horizontal surface to the lower horizontal surface, which shows good integrity and can better reflect the overall characteristics of the material. Therefore, the transverse section is mainly composed of β-fiber; however, the characteristic of H-component is not visible, which well reflects the rolling characteristics of sheet. Moreover, the orientation relationship of microtexture in BM is fixed; however, the change of observation surface leads to the change of the corresponding intensity distribution in EBSD results. Therefore, observing from 3D space and different surfaces can more comprehensively describe the microtexture and highlight its orientation characteristics. Moreover, the extensive deformation leads to the formation of low-angle grain boundaries and deformed grains, which then migrate and form sub-structure grains with the sufficient strain storage[19]. In the cold rolling process of thin sheet base metal, the deformation of surface in contact with cylinders is more intense, providing enough energy for the sub-structure grains formed by migration of low-angle grain boundaries, which can effectively release the severe strain in deformed grains. Therefore, the sub-structure grains are concentrated in the upper and lower horizontal planes of the sheet, and the deformed grains are mainly present in the middle part. In summary, the distribution of grain types in the BM exhibits the characteristic of regionalization.

Second, HAZ is the area where the BM is affected by the welding thermal cycle, whose microstructure has undergone certain evolutions compared with the BM. If energy attained from strain, heat input, and enough time is sufficient, in addition to occurrence of recrystallization, the sub-structure grains grow and merge into recrystallized grains due to the presence of a dynamically recovered sub-structure grain structure and sub-structure grain coalescence. For the HAZ, the welding thermal cycle provides a favorable condition for dynamic recrystallization and sub-structure grain formation and growth. As presented in Fig. 7~9 and Table 3, the increase in proportion of sub-structure and recrystallized grains and the decrease in proportion of deformed grains are a good proof. Furthermore, the increase in grain size of HAZ also indicates that the growth of sub-structure grain is dominant under the action of welding thermal cycle. The distribution of grain type in rolling thin sheet has obvious regional characteristics, which also leads to the regionalization of microstructure evolution of HAZ. The upper and lower horizontal surfaces are mainly sub-structure grain growth, and recrystallization mainly occurs in the middle part of HAZ, especially near the weld zone. This phenomenon can be better explained by the thermal history curves at different nodes in Fig. 4, revealing that the evolution of microstructure is more intense near the weld due to the high peak temperature and long high-temperature residence time. It is noted that while promoting the evolution of grain types, welding thermal cycle leads to the natural reduction in the intensity of original microtexture of the BM and produces new microtexture in the HAZ, such as cube-component.

Finally, it is found that the weld zone is mainly composed of equiaxed dendrite zone and fine equiaxed zone, and the preferred orientation of columnar zone decreases with the

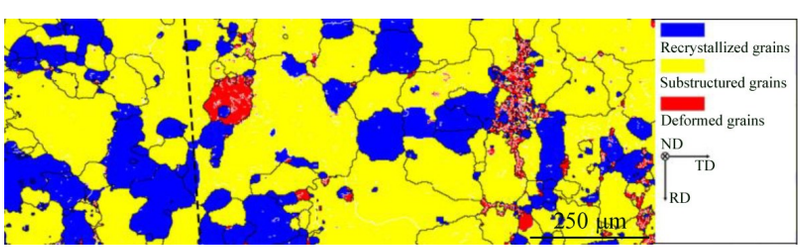

Fig.12 Grain morphologies maps of BM and HAZ from the lower horizontal surface of the joint with high-angle grain boundaries (>15°) and low-angle grain boundaries (2°~15°) marked in black and white lines, respectively

increase in distance from the upper horizontal surface. Therefore, microtexture of the weld zone is essentially random and the original microtexture of the BM is eliminated due to the re-melting of laser beam. Moreover, the longitudinal section located at the weld center line shows the excellent isotropic characteristic, and the isotropy is also observed in the equiaxed dendrite zone of other surfaces.

To sum up, the upper and lower horizontal surfaces expand individual microstructural characteristics in their respective regions. However, the transverse section shows popular characteristics of the joint. Therefore, it is necessary to study different surfaces of the joint to obtain the comprehensive and spatial understanding of microstructure. Moreover, the BM after cold rolling has significant layered distribution characteristic. The welding thermal cycle caused by laser beam is the fundamental source for the microstructure evolution in both WZ and HAZ, which makes the original microtexture characteristic of BM effectively weakened or even completely eliminated and the overall heterogeneity of the joint more complex. The heat input and strain rate provided by the thermal cycle are the driving forces of the microstructure evolution during laser welding process. Between them, the heat input plays a prominent role, and the effect of strain rate is extremely limited. Therefore, with the increase in laser welding heat input, the intensity of microstructure evolution inevitably increases, resulting in a wider distribution and a weaker microtexture characteristic of BM in both WZ and HAZ. Moreover, the microstructure evolution caused by increasing heat input not only weakens the role of precipitation strengthening in HAZ of the heat-treated aluminum alloy joint, but also intensifies the coarseness of grain size, which further reduce the strength of this region. In the meantime, increasing heat input also brings the similar issues for WZ, in which the loss of alloying elements and grain coarseness are the most prominent. On the one hand, the decrease in heat input can effectively prevent the softening caused by microstructure evolution. On the other hand, the strength enhancement and acute hardness gradient result in poor plasticity and damage tolerance of the joint. In summary, it is very significant to obtain a reasonable microstructure evolution by adjusting the thermal cycle to balance the strength and plasticity of the laser-welded Al-Li alloy joint.

4 Conclusions

1) For the base metal, obvious differences are observed in the grain morphology, orientation, and microtexture in the horizontal surfaces and the transverse section. The base metal exhibits distinct cold rolling microtexture, β-fiber, accompanied by a small amount of H-component located in the upper and lower horizontal surfaces. Moreover, the distribution of grain types in the base metal exhibits the localization characteristic. The upper and lower parts are dominated by sub-structure grains, and the middle part consists mainly of deformed grains.

2) For the heat affected zone, the welding thermal cycle provides a conducive condition for microstructural evolution including the formation and growth of dynamic recrystallization and sub-structure grains, and this phenomenon is more obvious at the regions closer to the weld. Moreover, this type of microstructural evolution not only weakens the original microtexture characteristics of the base metal, but also produces a new microtexture, i. e., cubic-component.

3) Microtexture of the weld zone is essentially random and the original microtexture of the base metal is eliminated due to the re-melting by laser beam. Moreover, some differences, such as weld zone size, grain distribution, grain morphology, and preferred orientation of columnar zone, are observed in different surfaces of the joint. The equiaxed dendrite zone shows good isotropy, especially in the central line of the weld.

4) The upper and lower horizontal surfaces expand individualized characteristics of microstructures in their respective regions. The transverse section shows popular characteristics of the joint. Therefore, systematic explorations for different surfaces of the joint are highly desirable to obtain the comprehensive and spatial understanding of microstructural characteristics.

References

1 Shao Y K, Li X Y, Chen L *et al*. *Metallurgical and Materials Transactions B*[J], 2021, 52(3): 1413

2 Wang Y C, Tong X, You G Q *et al*. *Rare Metal Materials and Engineering*[J], 2021, 50(3): 1069 (in Chinese)

3 Xue X L. *Rare Metal Materials and Engineering*[J], 2016, 45(12): 3319 (in Chinese)

4 Rioja R J, Liu J. *Metallurgical and Materials Transactions A*[J], 2012, 43(9): 3325

5 Tang Y C, Luo L, Luo L S *et al*. *Rare Metal Materials and Engineering*[J], 2019, 48(9): 2737

6 Shao Y K, Wang Y X, Yang Z B *et al*. *Acta Metallurgica Sinica*[J], 2017, 54(4): 547 (in Chinese)

7 Zhou B S, Liu F C, Huang C P *et al*. *Rare Metal Materials and Engineering*[J], 2018, 47(7): 2216 (in Chinese)

8 Viscusi A, Leito C, Rodrigues D M *et al*. *Journal of Materials Processing Technology*[J], 2016, 236: 48

9 Ma X Y, Duan A Q, Lu M *et al*. *Rare Metal Materials and Engineering*[J], 2017, 26(3): 1346

10 Hekmatjou H, Naffakh-Moosavy H. *Optics & Laser Technology*[J], 2018, 103: 22

11 Xiao R S, Zhang X Y. *Journal of Manufacturing Processes*[J], 2014, 16(2): 166

12 Kostrivas A, Lippold J C. *International Materials Reviews*[J], 1999, 44(6): 219

13 Lippold J C, Lin W. *Materials Science Forum*[J], 1996, 217: 1685

14 Cui L, Li X Y, He D Y *et al*. *Science and Technology of Welding and Joining*[J], 2013, 18(3): 204

15 Zhou D L, Chen X L, Xiao D W *et al*. *Rare Metal Materials and*

Engineering[J], 2008, 56(11): 2495 (in Chinese)
16 Perez M G, Kenik E A, O'Keefe M J *et al*. *Materials Science and Engineering A*[J], 2006, 424(1-2): 239
17 Voisin T, Forien J B, Perrom A *et al*. *Acta Materialia*[J], 2021, 203: 116 476
18 Lin D Y, Xu L Y, Jing H Y *et al*. *Additive Manufacturing*[J], 2020, 36: 101 591
19 Chen H Y, Fu L, Liang P. *Journal of Alloys and Compounds*[J], 2017, 692: 155
20 Zhang X, Zhou X, Hashimoto H *et al*. *Corrosion Science*[J], 2017, 116: 14
21 Zhang X X, Zhou X R, Hashimoto T *et al*. *Corrosion Science*[J], 2018, 132: 1
22 Zhang X X, Liu B, Zhou X R *et al*. *Corrosion Science*[J], 2018, 135: 177
23 Kouadri-Henni A, Seang C, Malard B *et al*. *Materials & Design*[J], 2017, 123: 89
24 Yang X W, Feng W Y, Li W Y *et al*. *Science and Technology of Welding and Joining*[J], 2018, 23(8): 704
25 Zhan X H, Mi G Y, Zhang Q *et al*. *The International Journal of Advanced Manufacturing Technology*[J], 2016, 88(9-12): 2537
26 Meng Q G, Fang H Y, Xu L W *et al*. *Transactions of the China Welding Institution*[J], 2006, 27(3): 9
27 Di X J, Xie H J, Chen C X *et al*. *Acta Metallurgica Sinica*[J], 2017, 30(12): 1
28 Shao Y K, Li X Y, Chen L *et al*. *Journal of Alloys and Compounds*[J], 2022, 895: 162 717
29 Sidor J J, Petrov R H, Lestens L A I. *Materials Characterization*[J], 2011, 62(2): 228
30 Attarilar S, Ebrahimi M, Hsieh T H *et al*. *Materials Science and Engineering A*[J], 2021, 803: 140 489
31 Kumar R, Gupta A, Dandekar T R *et al*. *Intermetallics*[J], 2021, 130: 107 064
32 Chen X R, Zheng Z Q, Ye Z H *et al*. *Rare Metal Materials and Engineering*[J], 2016, 47(6): 1786

2A97-T3铝锂合金激光焊接接头微观组织与织构的EBSD研究

邵盈恺[1]，李晓延[1]，陈　俐[2]，嵇　罡[3]
(1. 北京工业大学 材料与制造学部，北京 100124)
(2. 中国航空制造技术研究院，北京 100124)
(3. 里尔大学 法国国家科学研究中心 国立农业、食品和环境研究所 中央理工大学，法国 里尔 F-59000)

摘　要：从2A97-T3铝锂合金激光焊接头的上水平面、横截面、纵截面和下水平面进行取样，对接头的微观组织和织构进行了分析。利用电子背散射衍射（EBSD）技术的多种表征方法，如OIM、PF、IPF、取向角分布、ODF、晶粒形貌图，并结合激光焊过程的数值模拟，研究了激光焊作用下接头微观组织的演变机理。结果表明，由于薄板冷轧工艺和激光焊加工的非平衡特性，导致接头不同截面的晶粒形态、取向和微观织构存在明显差异。这种组织的不均匀性是接头性能各向异性的根本来源。因此，有必要对接头的不同截面进行分析，进而对微观组织和织构获得全面性和空间性的认识。激光诱导下，热影响区发生了动态再结晶和亚结构晶粒的形成和长大，焊缝区则产生了微观组织的重熔现象，该过程会导致母材原有织构特征在热影响区减弱、在焊缝区消失。

关键词：激光焊；铝锂合金；EBSD；微观组织；织构

作者简介：邵盈恺，男，1992年生，博士，北京工业大学材料与制造学部，北京 100124，E-mail：syk@emails.bjut.edu.cn